Check for updates

Short-Wave Infrared Colloidal QD Photodetector with Nanosecond Response Times Enabled by Ultrathin Absorber Layers

Yu-Hao Deng,* Chao Pang, Ezat Kheradmand, Jari Leemans, Jing Bai, Matthias Minjauw, Jiayi Liu, Korneel Molkens, Jeroen Beeckman, Christophe Detavernier, Pieter Geiregat, Dries Van Thourhout, and Zeger Hens*

Ultrafast short-wavelength infrared (SWIR) photodetection is of great interest for emerging automated vision and spatial mapping technologies. Colloidal quantum dots (QDs) stand out for SWIR photodetection compared to epitaxial (In,Ga)As or (Hg,Cd)Te semiconductors by their combining a size-tunable bandgap and a suitability for cost-effective, solution-based processing. However, achieving ultrafast, nanosecond-level response time has remained an outstanding challenge for QD-based SWIR photodiodes (QDPDs). Here, record 4 ns response time in PbS-based QDPDs that operate at SWIR wavelengths is reported, a result reaching the requirement of SWIR light detection and ranging based on colloidal QDs. These ultrafast QDPDs combine a thin active layer to reduce the carrier transport time and a small area to inhibit slow capacitive discharging. By implementing a concentration gradient ligand exchange method, high-quality p–n junctions are fabricated in these ultrathin QDPDs. Moreover, these ultrathin QDPDs attain an external quantum efficiency of 42% at 1330 nm, due to a 2.5-fold enhanced light absorption through the formation of a Fabry–Perot cavity within the QDPD and the highly efficient extraction (98%) of photogenerated charge carriers. Based on these results, it is estimated that a further increase of the charge-carrier mobility can lead to PbS QDPDs with sub-nanosecond response time.

1. Introduction

Light in the short-wave infrared window (SWIR, 1000–3000 nm) is far less affected by scattering than visible light, thereby offering a long effective detection distance even under difficult weather conditions or in biological tissue.[1–3] Moreover, through vibrational overtones, SWIR light provides much more chemical information about objects than visible light in an imaged scene,[4] while being safer for the human eye. Therefore, detection of SWIR light is not only the cornerstone of optical communications, but also of remote sensing and automated vision technologies, biological imaging, environmental monitoring, and spectroscopy.[5–9] In particular in light detection and ranging (LiDAR) – a 3D imaging approach based on time of flight (ToF) – SWIR detection can make possible the detection and identification of obstacles, and spatial mapping technologies for autonomous driving, facial recognition, and virtual/augmented reality. However, for 3D imaging with high spatial

Y.-H. Deng, E. Kheradmand, J. Leemans, J. Bai, K. Molkens, P. Geiregat, Z. Hens
Physics and Chemistry of Nanostructures Group
Ghent University
Ghent 9000, Belgium
E-mail: yuhao.deng@ugent.be; zeger.hens@ugent.be
Y.-H. Deng, C. Pang, E. Kheradmand, J. Leemans, J. Bai, J. Liu, K. Molkens, J. Beeckman, P. Geiregat, D. Van Thourhout, Z. Hens
Center for Nano and Biophotonics
Ghent University
Ghent 9052, Belgium

C. Pang, K. Molkens, D. Van Thourhout
Photonics Research Group
Ghent University
Ghent 9052, Belgium
M. Minjauw, C. Detavernier
Department of Solid State Sciences
Ghent University
Ghent 9000, Belgium
J. Liu, J. Beeckman
Department of Electronics and Information Systems
Ghent University
Ghent 9052, Belgium

**ADVANCED
SCIENCE NEWS**

www.advancedsciencenews.com

**ADVANCED
MATERIALS**

www.advmat.de

resolution and high frame rates, ultrafast photodetectors with response times of nanoseconds or less are paramount.[10,11] SWIR sensors currently on the market involve a heterogeneous technology in which a SWIR sensitive semiconductor – typically (In,Ga)As or (Hg,Cd)Te – is combined with a silicon read-out circuit. While offering performing SWIR cameras, the use of such epitaxial materials and the need for cumbersome integration steps, make this technology ill-suited for high-volume, low-cost deployment in 3D imaging.[10,12–14]

Recently, colloidal quantum dots (QDs) have emerged as promising printable semiconductors with size-tunable optical properties that can be applied in a new generation of electronic and optoelectronic devices. Here, QDs offer cost-effective, solution-based processing, instead of traditional costly, high-vacuum, and high-temperature epitaxial growth,[15–19] where a highly promising direction involves the replacement of epitaxial single crystals by QDs for detection of SWIR light.[12] In particular for photodiode stacks using PbS QDs as the photoactive layer, external quantum efficiencies (EQEs) of 60% or more have been demonstrated at SWIR wavelengths.[20] For such stacks, a response time of 70 ns was reported already in 2009.[21] Replacing organic by inorganic halide ligands – which typically enhance charge-carrier mobility – a further reduction of the response time to 10 ns was reported only recently.[22] This step was achieved by optimizing quantum dots photodiode (QDPD) stacks made of 420 nm thick PbS QD films for fast carrier extraction and minimizing the QDPD area. Similar results have not yet been obtained by recent work on alternative SWIR QDs, such as In(As,P),[13,23] InSb QDs,[24,25] or Ag$_2$Te,[26] which yielded QDPDs with response times ranging from ≈1 to 7.3 μs, or even 500 ms. It thus appears that obtaining an ultrafast, nanosecond-level photoresponse remains a major obstacle for implementing QDPDs for SWIR photodetection.

Here, we report the formation of PbS-based QDPDs operating at SWIR wavelengths for which the response time is reduced by limiting the active layer thickness. We fabricate PbS QD films with an active layer thickness down to 50 nm by means of a gradual transition between ligand exchange methods know to produce n- and p-type PbS QD films, thereby avoiding any in situ change in doping-type during film deposition. Even for only 50 nm thick active layers, the resulting stacks exhibit a pronounced rectification and attain an EQE of 42% at 1330 nm under a bias voltage of −1 V. We argue that this result is obtained through a combination of enhanced absorption in the PbS QD film by the QDPD stack forming a Fabry–Pérot cavity and the efficient carrier extraction from the thin QD film, which leads to an internal quantum efficiency of 98%. Importantly, by reducing the device area to 50 μm diameter circles, the devices feature a fall time of 4 ns under pulsed illumination using a 1030 nm femtosecond laser. This result shows that reducing the active layer thickness is a viable path toward realizing ultrafast QDPDs in the SWIR, where in particular a further increase of the charge carrier mobility can lead to sub-nanosecond response times.

2. Results and Discussion

2.1. Response Time Estimation

Current PbS QDPDs are typically formed using an internal p–n junction in which a p-PbS QD layer contacts an n-PbS QD layer. Various doping densities have been reported in the literature for these layers, with most numbers varying between 10^{15} and 10^{17} cm^{-3}.[27–29] The response time τ_{res} of such a QDPD is seen as the rise time or fall time required for the photocurrent to change from 10% to 90% of its final value or vice versa. Both rise and fall times are typically described as a combination of the time needed to collect photogenerated carriers at the electrodes through (τ_{drift}) drift and (τ_{diff}) diffusion within this p–n junction and the time (τ_{RC}) to pass these carriers through the external circuit[12,30]

$$\tau_{res} = \sqrt{\tau_{drift}^2 + \tau_{diff}^2 + 2.2\tau_{RC}^2} \tag{1}$$

Here, factor 2.2 is added since the response time involves the variation of the photocurrent between 10% and 90% of the maximal value. Clearly, τ_{res} is dictated by the slowest process.

A first step to accelerate the response time is the elimination of charge-carrier diffusion, which can be brought about by forming a fully depleted PbS QD film. As outlined in Figure S1 (Supporting Information), a regime of full depletion is expected for a 100 nm thick film with a doping density of 10^{16} cm^{-3} under reverse bias. To make a best-case estimate of the impact of the QDPD design on the response time, we therefore considered a simplified description of the device, as shown in **Figure 1a**. The figure displays a fully depleted QD film, in which the electric field is determined by charges at the n-type and p-type contact. In such a structure, photogenerated electrons and holes drift under the action of the electric field to opposite sides of the QD film, from where they are transferred to the external circuit. As outlined in Figure S2 (Supporting Information), the photocurrent under drift-limited conditions after pulsed illumination drops to zero after a collection time τ_{drift} given by

$$\tau_{drift} = \frac{d^2}{\mu V} \tag{2}$$

Here, d is the layer thickness, μ the charge carrier mobility and V is the voltage drop across the depleted film. Figure 1b displays τ_{drift} as a function of d according to Equation (1) assuming a voltage drop of 1 V and a mobility of 4×10^{-2} cm^2 V^{-1} s^{-1}. Such a voltage drop is easily obtained under reverse bias, while the assumed mobilities agree with experimental data on the PbS QD films used in this study, see later. As can be seen, such a combination of voltage drop and mobility yields a drift time of 62.5 ns for 500 nm, and 2.5 ns for 100 nm thick films.

In combination with the drift of photogenerated carriers, the dynamic response of a QDPD is determined by the time needed to transfer charge carriers through the external circuit, which depends on the capacitance C_S and the series resistance R_S of the QDPD stack. Considering the depleted n-type layer as a parallel plate capacitor, the resulting time constant τ_{RC} is given by

$$\tau_{RC} = R_S C_S = R_S \frac{\varepsilon_0 \varepsilon_r A}{d} \tag{3}$$

Here, ε_0 is the permittivity of the vacuum, and ε_r and A the dielectric constant and the area of the PbS QD film. Figure 1c represents the response time according to Equations (1)–(3) as a
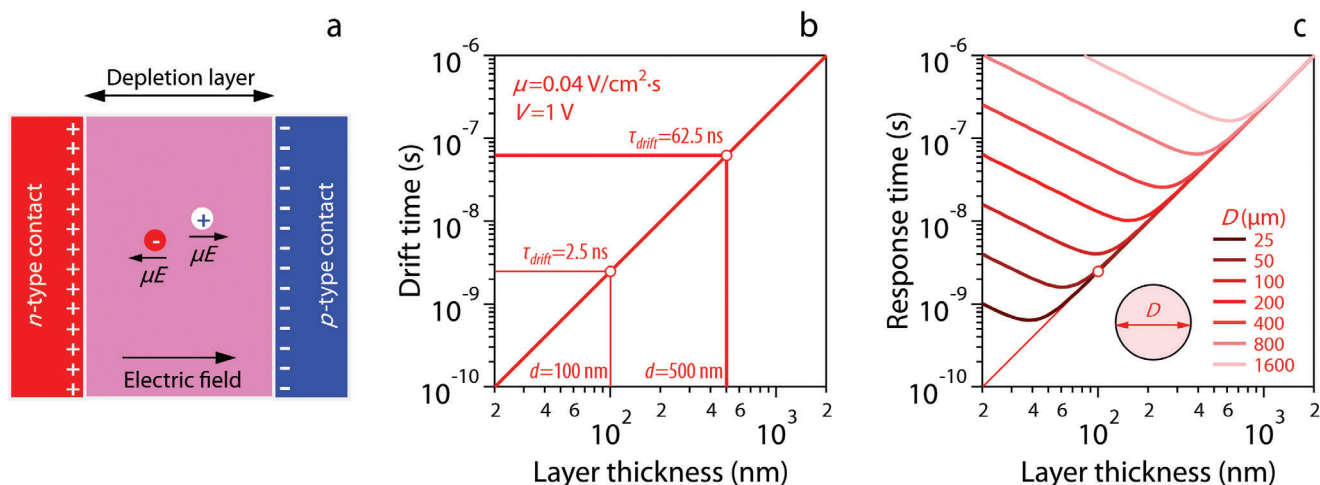
Figure 1. Response time estimation. a) Scheme of a fully depleted photoactive layer, for which the mobility µ and the electric field $E = V/d$ determine the drift time. b) Drift time versus layer thickness calculated according to Equation (1) for a charge carrier mobility and an applied voltage difference as indicated. c) Calculated response time as a function of layer thickness for different electrode areas, as characterized by the electrode diameter D. Calculations done according to Equations (1)–(3), using a series resistance R_S of 200 Ω and a dielectric constant $\epsilon_r = 15.5$.

function of the layer thickness, taking $\epsilon_r = 15.5$,[12] and assuming a fixed series resistance $R_S = 200$ Ω, two estimates in line with literature reports.[12,22] The figure highlights that drift will limit the response of thicker devices, while τ_{RC} will determine the response time for thinner devices. The balance between both, however, strongly depends on the device area. Even so, Figure 1c highlights that, given the assumed charge carrier mobility and series resistance, response times of a few nanoseconds remain feasible when using contact electrodes with a diameter of 50 µm or less.

2.2. PbS QD Film Formation

In this work, we formed QDPDs with thin absorber layers by sandwiching a film of n-type PbS QDs with a bandgap absorption at 1330 nm between n-ZnO and a film of p-type PbS QDs with a bandgap absorption at 950 nm. As outlined in the Experimental Section and Figure S3 (Supporting Information), PbS QDs were synthesized by reacting lead oleate and a substituted thiourea according to a synthesis method described in the literature.[31] As shown in **Figure 2a,b**, we obtained PbS QD layers exhibiting n-type or p-type character by exposing a spin-coated film of the as-synthesized QDs to either tetrabutylammonium iodide (TBAI) or ethanedithiol (EDT), respectively. Using field-effect transistor (FET) measurements, see Figure S4 in the Supporting Information, the electron mobility in TBAI-treated films was estimated between 8.22×10^{-3} and 7.25×10^{-2} cm^2 V^{-1} s^{-1} according to the forward and backward sweep of the gate voltage. Similarly, hole mobilities in these films were estimated at 8.12×10^{-3} and 2.26×10^{-2} cm^2 V^{-1} s^{-1}, respectively. Note that these figures should be seen as lower limits, since any film imperfection will lower the source–drain current, and the analysis assumes that a change in gate voltage only changes the mobile charge in the QD film.

Diode stacks formed by the sequential deposition of a 50 nm n-type and a 50 nm p-type PbS QD layers (see Figure 2a, Method 1)

on an indium tin oxide (ITO)/ZnO substrate showed a considerable dark current of 2.41 mA cm^{-2} at -1 V reverse bias, and a $+1/-1$ V rectification ratio of only 2.93, see Figure 2c. Further data on this initial stack are summarized in Figure S5 (Supporting Information). We conjectured that the abrupt switch from TBAI to EDT exposure to form a p–n junction is problematic within an ultrathin PbS QD stack, since EDT exposure of the upper film could leach away iodide from the underlying PbS/TBAI film,[32] thereby undoing the n-type doping. As shown in Figure S6 (Supporting Information), elemental analysis prior to and after exposing a PbS/TBAI film to EDT indeed indicated a loss of iodide from the film, and field-effect transistor measurements confirm that such films have p-type character. In order to preserve a p–n junction in the PbS QD film, we therefore proceeded by reducing the thickness of each deposited film of the as-synthesized PbS QDs, while gradually increasing the concentration of the EDT bath upon switching from TBAI to EDT exposure, see Method 2 in Figure 2a. In doing so, we assumed that the densification of the PbS QD film would prevent the leaching of iodide once the switch to the highest concentration EDT baths was made. As illustrated in Figure 2c, this approach improved considerably the characteristics of the QDPD, which featured after the evaporation of a gold top contact a dark current of 4.18 µA cm^{-2} at -1 V reverse bias, and a $+1/-1$ V rectification ratio of 1630.

2.3. Photodiode Characterization as a Function of Stack Design

In order to evaluate the relation between the stack design parameters – layer thickness and device area – and the photodiode characteristics, we fabricated QDPDs by sandwiching the n-PbS(TBAI)/p-PbS(EDT) QD layer between a glass/ITO/ZnO electrode as the n-type contact and a gold electrode as the p-type contact, see **Figure 3a**. Details on the fabrication process are provided in the Experimental Section. Figure 3b shows a scanning electron microscopy cross-section of an actual device stack, featuring an n-PbS/p-PbS QD film with a total thickness of

**ADVANCED
SCIENCE NEWS**

www.advancedsciencenews.com

**ADVANCED
MATERIALS**

www.advmat.de
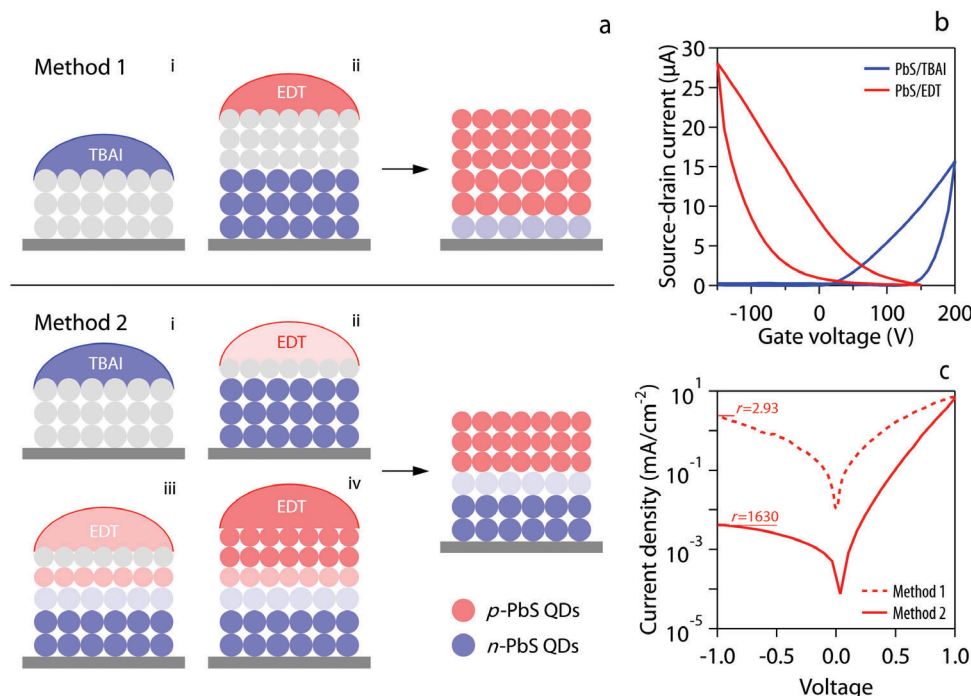
Figure 2. a) Depiction of the different methods used to fabricate a stack of ultrathin n-PbS and p-PbS QDs, indicating in Method 1 the conjecture that an abrupt switch from TBAI to EDT turns the underlying n-PbS film into a p-PbS layer and displaying the gradual increase in EDT concentration in Method 2. b) Transfer curves for PbS QD films treated with (blue) TBAI and (red) EDT, highlighting the n- and p-type characters of the films. Mobilities were estimated from the maximal slopes in the forward and backward sweep directions. c) Dark current measured on QDPDs consisting of 50 nm n-type and 50 nm p-type QD films, fabricated according to Methods 1 and 2, as indicated.

100 nm, while the inset shows an optical microscopy image of a QDPD chip featuring circular gold contacts pads with diameters ranging from 500 to 20 μm. Because of practical limitations, only pads with a diameter up to 50 μm could be contacted.
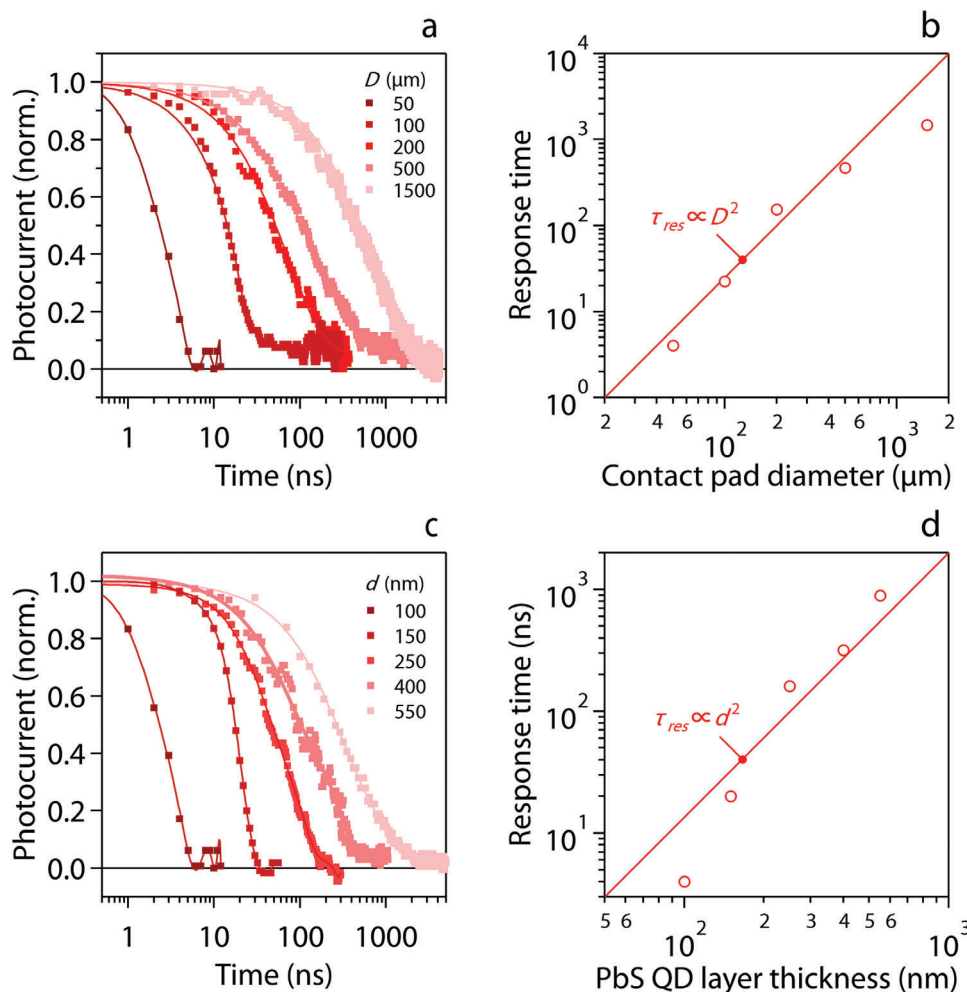
Figure 3c represents the current–voltage characteristics of a QDPD with a 50 nm thick photoactive layer, illuminated at 1030 nm. As can be seen, an almost bias-independent photocurrent is obtained. Interestingly, the external quantum efficiency η_{ext} peaks at 42% at ≈1330 nm, a wavelength corresponding to

the bandgap transition of the n-PbS QDs, see Figures 3d and S3 in the Supporting Information. As shown in Figure S7 (Supporting Information), this remarkably high EQE is brought about by the QDPD stack forming a Fabry–Pérot cavity.[33,34] More precisely, we estimate that the light absorbed by a 50 nm QD film at 1330 nm increases from 16.56% for a film on glass to 42.06% for the same film within the QDPD, i.e., a 2.5-fold enhancement. We confirmed this calculation experimentally by reflection measurements, thereby subtracting the reflection of the QDPD stack
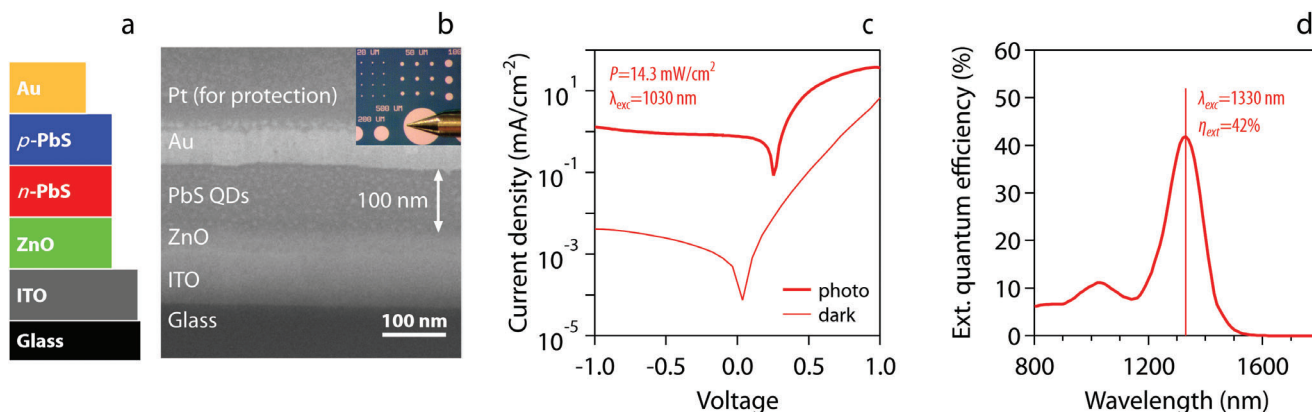
Figure 3. a) Diagram outlining the cross-section of the intended QDPD stack. b) Scanning electron microscopy image of the cross-section of an actual QDPD stack. The inset displays part of a QDPD chip, showing gold pads for contacting with diameters changing from 20 to 500 μm. c) Current–voltage characteristics in the dark and under illumination, using power and wavelength as indicated. d) Spectrum of the external quantum efficiency η_{ext} of the QDPD stack, highlight the maximum η_{ext} recorded at 1330 nm.

ADVANCED
SCIENCE NEWS

www.advancedsciencenews.com

**ADVANCED
MATERIALS**

www.advmat.de

Figure 4. a) Transient photocurrent after illumination using a 100 fs, 1030 nm laser pulse of 100 nm thick QDPDs formed using contact pads of varying radii as indicated. The thin lines are interpolations of the transient used to determine the response time. b) Response time as a function of the contact pad diameter. The full line represents a $\tau_{res} \propto D^2$ trendline, in line with the relation expected for τ_{RC}. c) Transient photocurrent for QDPDs formed using 50 µm contact pads with QD films of varying thicknesses. d) Response time as a function of QD layer thickness. The full line represents the $\tau_{res} \propto d^2$ relation expected for τ_{drift}.

from that of the Au/ITO substrate, which yielded a comparable absorbance at 1335 nm of 42.7%, see Figure S7 in the Supporting Information. Such an absorbance yields an internal quantum efficiency η_{int} of 98% at 1330 nm, a result that underscores the efficient charge carrier extraction from the ultrathin PbS QDPDs introduced here. Assuming shot noise as the dominant contribution to the detector noise, we estimate from these numbers a detectivity at 1330 nm of 3.9×10^{11} cm Hz$^{0.5}$ W^{-1}, see Figure S8 in the Supporting Information.

As shown in Figure S9 (Supporting Information), a QDPD stack with a 100 nm PbS QD bilayer features a constant capacitance of ≈ 75 nF cm^{-2} up to a forward bias of 0.35 V, in agreement with the assumption of a fully depleted film. We therefore evaluated the dynamic response of the QDPDs by measuring the photocurrent transient at 0 V bias under pulsed illumination using a 1030 nm, 100 fs laser. **Figure 4a** shows a series of such transients recorded on QDPDs with a 100 nm thick n-PbS(TBAI)/p-PbS(EDT) absorber layer contacted using circular

gold pads with diameters decreasing from 1500 to 50 µm. As can be seen, we observed a systematic shortening of the photocurrent response upon reducing the area of the contact pad. More quantitatively, we interpolated the transients, as shown in Figure 4a and identified the response time τ_{res} with the time needed for the photocurrent to drop between 90% and 10% of the maximal value, a typical definition of the fall time. Interestingly, we found that τ_{res} reduces from 1.48 µs for the $D = 1500$ µm contact to 4 ns for the $D = 50$ µm contact. This reduction agrees largely with the expected scaling of τ_{RC} with the contact pad area, see Equation (3) and Figure 4b. For completeness, we also analyzed the frequency response of the $D = 200$ µm QDPD, which yielded a 3 dB bandwidth in agreement with the measured response time, see Figure S10 in the Supporting Information.

Interestingly, for the smallest contact pads, the response time of 4 ns agrees with the expectations for drift-limited transport through a depleted QD film, which suggests that in that

**ADVANCED
SCIENCE NEWS**

www.advancedsciencenews.com

**ADVANCED
MATERIALS**

www.advmat.de
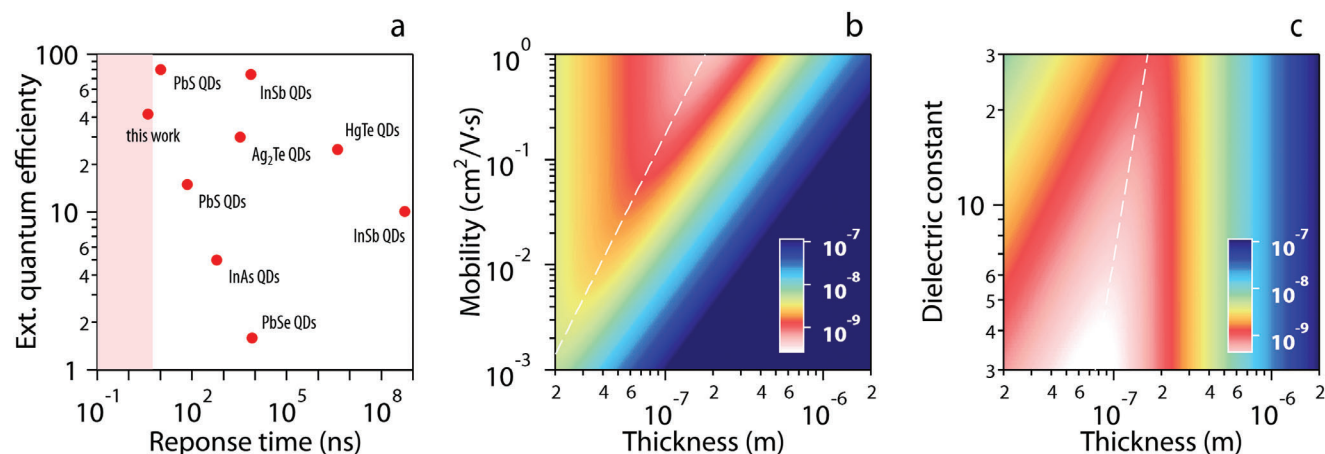
Figure 5. Analysis of response times. a) Diagram comparing the QDPD reported in this work with state-of-the-art devices in terms of EQE and response time. Only QDPDs active within the SWIR are included. b) Response time as a function of photoactive layer thickness and mobility, determined for $\varepsilon_r = 15.5$, $D = 50\,\mu m$, $V = 1\,V$, and $R_S = 200\,\Omega$. The dashed line indicates the thickness with the shortest response time for each given mobility. c) Response time as a function of photoactive dielectric constant, determined for $\mu = 0.04\,cm^2\,V^{-1}\,s^{-1}$, $D = 50\,\mu m$, $V = 1\,V$, and $R_S = 200\,\Omega$. The dashed line indicates the thickness with the shortest response time for each given dielectric constant.

case, τ_{RC} is no longer limiting the time response. To analyze this point further, Figure 4c represents current transients recorded on QDPDs contacted through $D = 50\,\mu m$ gold pads, for which the thickness of the n-PbS(TBAI) film was increased from 50 to 200 and 500 nm. While such a change reduces τ_{RC}, we find that the response time strongly increases for thicker films, a result suggesting that τ_{res} is indeed determined by charge carrier transport. Moreover, as shown in Figure 4d, the increase of τ_{res} is more pronounced than the d^2 scaling expected for drift-limited transport. This result suggests that thicker films under 0 V bias are most likely not fully depleted, such that carrier transport involves a combination of diffusion and drift. Even so, the 4 ns response time obtained here for a 100 nm thick QDPD contacted with a $D = 50\,\mu m$ gold pad is the shortest response time reported for QDPDs active in the SWIR. We thus conclude that ultrathin absorber layers can greatly improve the response of QDPDs, down to a few nanoseconds.

3. Discussion

Figure 5a compares the performance of the QDPD presented here with state-of-the-art SWIR-active QDPDs in terms of EQE and response time. The shaded area delineates nanosecond-level response times needed for LiDAR applications with submeter spatial resolution and gigahertz frame rates. As can be seen, the 3.9 ns response time, which we achieved by reducing the thickness of the photoactive layer, brings QDPDs at the edge of what is needed for such a ToF-based application. Moreover, the reasonable agreement between the predicted and measured relation between response time and QDPD design parameters enables us to outline next steps for further reducing the response time of SWIR-active QDPDs. In order to do so, we use Equations (1)–(3) to write the thickness d_{opt} that minimizes the response time for a given set of film parameters as

$$d_{opt} = 1.1^{1/6} \left(R_S \varepsilon_0 \varepsilon_r A \mu V \right)^{1/3} \qquad (4)$$

Using this expression, the shortest response time τ_{min} reads

$$\tau_{min} = \frac{\sqrt{3.3} \left(R_S \varepsilon_0 \varepsilon_r A \right)^{2/3}}{(\mu V)^{1/3}} \qquad (5)$$

Based on these relations, a first parameter that can be changed for obtaining faster QDPDs is the charge carrier mobility. Figure 5b displays the response time as a function of film thickness and mobility. Increasing the charge carrier mobility as compared to the $\approx 4 \times 10^{-2}\,cm^2\,V^{-1}\,s^{-1}$ for the films used in this study will further reduce τ_{drift}, and make the response time increasingly dominated by τ_{RC}. Hence, the optimal layer thickness for a fast QDPD response will increase due to the concomitant reduction of the capacitance and τ_{min} will drop, see Equations (4) and (5) and Figure 5b. Interestingly, higher mobility films can therefore compensate for the reduced absorption by the ultrathin photoactive layers introduced here. Enhancing mobility could be achieved by either reducing the QD–QD interdistance, or improving the passivation of defects that trap charge carriers.

According to Equation (5), reducing the dielectric constant provides a second pathway to lower the response time of a QDPD. The smaller capacitance of a smaller dielectric constant film lowers τ_{RC}, such that the response of thinner films can remain controlled by drift. However, this balance makes that even thinner films are needed to obtain the shortest response time, which will lower the absorption by the film. Hence, exploring QDs with a lower dielectric constant than PbS, such as InAs QDs, is an option for making faster QDPDs, provided that films with sufficient charge-carrier mobility can be formed – which allows for fast response times in thicker films.

4. Conclusion

In summary, we demonstrate the record ultrafast SWIR colloidal QD photodetector with 4 ns response time and near-limiting internal quantum efficiency of 98% by applying an ultrathin structure design and inhibiting limitation by capacitive discharging.

**ADVANCED
SCIENCE NEWS**

www.advancedsciencenews.com

**ADVANCED
MATERIALS**

www.advmat.de

This nanosecond-level response attains the application requirements of SWIR LiDAR with submeter spatial resolution and gigahertz frame rates based on colloidal QDs. This result was obtained by realizing ultrathin PbS QD p–n junctions through a concentration gradient ligand exchanged method that inhibits iodide removal during fabrication. The resulting photodiodes attain a +1/−1 V rectification ratio of 1600 rectification ratio and exhibit an external quantum efficiency of 42%. Such a high efficiency results from the formation of a Fabry–Perot cavity within the photodiode stack, and the highly efficient charge carrier extraction. Based on these results, we discuss directions to further reduce the response time. As such, this work expands the potential applications of SWIR colloidal QD photodetection in ultrafast detection, such as LiDAR, optical communications, ultrafast imaging, real-time environmental monitoring, and diagnosis technology.

5. Experimental Section

Synthesis of 950 nm PbS QDs: Lead oleate and *N*-(3,5-bis(trifluoromethylphenyl))-*N′*-phenylthiourea precursors were synthesized according to Hendricks et al.[31] 7.00 mmol of lead oleate was dissolved in 25 mL of anhydrous *n*-octane in a flask at 90 °C under a nitrogen atmosphere. In a separate vial, 4.67 mmol of *N*-(3,5-bis(trifluoromethylphenyl))-*N′*-phenylthiourea was mixed with 2 mL of diglyme and heated to 90 °C. The thiourea solution was then rapidly injected into the lead oleate solution using a syringe. After 1 min of reaction time, the flask was quickly cooled to ambient temperature by immersing it in a water bath. The resulting dispersion underwent a four-cycle purification process using *n*-octane and acetone, and was subsequently stored in anhydrous *n*-octane for future applications.

Synthesis of 1300 nm PbS QDs: 2 mmol of lead oleate was dissolved in 20 mL of *n*-dodecane in a flask and kept 30 min at 120 °C under a nitrogen atmosphere. Subsequently, 1.5 mmol of the thiourea precursor (*N*-(*p*-(trifluoromethyl)phenyl)-*N′*-dodecylthiourea) was combined with 1 mL of diglyme. This mixture was also maintained under a nitrogen atmosphere, preheated to 120 °C, and then rapidly introduced into the previously prepared lead oleate solution. After 80 s, the reaction mixture was allowed to cool to ambient temperature by placing the flask in a water bath. The resultant dispersion underwent a minimum of four purification cycles using octane and acetone followed by filtering using a 0.45 μm pore size syringe filter. Finally, the dispersion was reconstituted in anhydrous *n*-octane to achieve the desired 50 mg mL⁻¹ concentration.

Preparation of ZnO nanocrystals (NCs): ZnO NCs were synthesized following standard method as described in the literature.[35] ZnO NCs were dispersed in a solution of 2% butylamine in chloroform with a concentration of 40 mg mL⁻¹. The ZnO NC solution was filtered through a filter (0.45 μm) and stored in the refrigerator for future use.

Fabrication of QD Photodiode: Before fabrication, the ITO glass was ultrasonically cleaned with acetone, ethanol, and deionized water, then treated with O_2 plasma. ZnO NCs in chloroform (40 mg mL⁻¹) were spun on top of the substrate with a spin speed of 2500 rpm. The PbS QD solution was then deposited on the ZnO layer via a layer-by-layer method, where for each layer, 40 μL of the QD solution was dropped and spun at 2500 rpm for 30 s. Oleate-capped QDs were electrically insulating and the ligands had to be replaced by shorter ligands. For the PbS–TBAI layer, TBAI solution (10 mg mL⁻¹ in methanol) was applied to the substrate for 30 s and spun at 2500 rpm for 10 s, followed by 2 times acetonitrile rinse. Whereas the concentration gradient ligand exchanged method for the EDT-exchanged PbS layer, the first layer was used with 25 mg mL⁻¹ QDs and EDT solution (0.005 vol % in acetonitrile), the second layer was used with 25 mg mL⁻¹ QDs and EDT solution (0.01 vol % in acetonitrile), and the third layer was used with 50 mg mL⁻¹ QDs and EDT solution (0.02 vol % in acetonitrile), then annealing and vacuum treatment were

also applied. Finally, Au (120 nm) was thermally evaporated on the PbS film.

Device Characterization: Capacitance–voltage curves were measured by the HP4192ALF impedance analyzer. *J–V* measurements were taken using a sourcemeter (Keithley 2400) under N_2 atmosphere. Wavelength-dependent EQE was measured with a quantum efficiency measurement system (Newport Inc.) using a commercial Ge detector as reference. The temporal response of each photodetector was evaluated by measuring the transient photocurrent (TPC) recorded with a 1 GHz oscilloscope (DSO8104A Infinium, Agilent) while a 150 fs pulsed laser (PHAROS, Light Conversion) with a 200 kHz repetition rate illuminated each individual photodetector pixel. All reported TPC experiments were done using a 1030 nm excitation without external bias across the device. X-ray photoelectron spectroscopy (XPS) was measured using a Thermo Scientific K-Alpha system for exchanged QDs deposited on ITO/glass substrates. Scanning electron microscopy images were obtained by a Hitachi S-5200 microscope. The optical absorption measurements under reflection mode were performed with a Perkin-Elmer Lambda 950 UV–vis–near infrared (NIR) spectrophotometer. Field-effect transistor measurements were carried out on QD films cast onto degenerately doped silicon substrates that were coated with a 300 nm thick thermal SiO_2 gate oxide and patterned with source/drain electrodes (8×25 μm channel width, 4 μm length). The structure of FET is shown in Figure S4 (Supporting Information). The linear mobilities were calculated according to equation $\mu = dI_{DS}/dV_{GS}V_{DS} \, L/WC_{ox}$ and an intrinsic gate capacitance C_i of 1.15×10^{-8} F cm⁻².[13]

Supporting Information

Supporting Information is available from the Wiley Online Library or from the author.

Conflict of Interest

The authors declare no conflict of interest.

Data Availability Statement

The data that support the findings of this study are available on request from the corresponding authors. The data are not publicly available due to privacy or ethical restrictions.

[1] M. P. Hansen, D. S. Malchow, presented at Thermosense XXX, FL, USA, **2008**, https://doi.org/10.1117/12.777776.

[2] E. Thimsen, B. Sadtler, M. Y. Berezin, *Nanophotonics* **2017**, *6*, 1043.

[3] O. T. Bruns, T. S. Bischof, D. K. Harris, D. Franke, Y. Shi, L. Riedemann, A. Bartelt, F. B. Jaworski, J. A. Carr, C. J. Rowlands, M. W. B. Wilson, O. Chen, H. Wei, G. W. Hwang, D. M. Montana, I. Coropceanu, O. B. Achorn, J. Kloepper, J. Heeren, P. T. C. So, D. Fukumura, K. F. Jensen, R. K. Jain, M. G. Bawendi, *Nat. Biomed. Eng.* **2017**, *1*, 0056.

[4] F. P. García de Arquer, D. V. Talapin, V. I. Klimov, Y. Arakawa, M. Bayer, E. H. Sargent, *Science* **2021**, *373*, eaaz8541.

[5] T. Rauch, M. Böberl, S. F. Tedde, J. Fürst, M. V. Kovalenko, G. Hesser, U. Lemmer, W. Heiss, O. Hayden, *Nat. Photonics* **2009**, *3*, 332.

[6] Z. Ren, J. Sun, H. Li, P. Mao, Y. Wei, X. Zhong, J. Hu, S. Yang, J. Wang, *Adv. Mater.* **2017**, *29*, 1702055.

[7] X. Tang, M. M. Ackerman, M. Chen, P. J. N. Guyot-Sionnest, *Nat. Photonics* **2019**, *13*, 277.

[8] D. Shin, F. Xu, D. Venkatraman, R. Lussana, F. Villa, F. Zappa, V. K. Goyal, F. N. C. Wong, J. H. Shapiro, *Nat. Commun.* **2016**, *7*, 12046.

[9] J. Yu, J. Zheng, H. Chen, N. Tian, L. Li, Y. Qu, Y. Huang, Y. Luo, W. Tan, *J. Mater. Chem. C* **2022**, *10*, 274.

[10] B. Sun, A. M. Najarian, L. K. Sagar, M. Biondi, M. J. Choi, X. Li, L. Levina, S. W. Baek, C. Zheng, S. Lee, A. R. Kirmani, R. Sabatini, J. Abed, M. Liu, M. Vafaie, P. Li, L. J. Richter, O. Voznyy, M. Chekini, Z.-H. Lu, F. P. García de Arquer, E. H. Sargent, *Adv. Mater.* **2022**, *34*, 2203039.

[11] M. Park, Y. Baek, M. Dinare, D. Lee, K.-H. Park, J. Ahn, D. Kim, J. Medina, W.-J. Choi, S. Kim, C. Zhou, J. Heo, K. Lee, *Sci. Rep.* **2020**, *10*, 2764.

[12] Q. Xu, L. Meng, K. Sinha, F. I. Chowdhury, J. Hu, X. J. A. P. Wang, *ACS Photonics* **2020**, *7*, 1297.

[13] J. Leemans, V. Pejović, E. Georgitzikis, M. Minjauw, A. B. Siddik, Y. H. Deng, Y. Kuang, G. Roelkens, C. Detavernier, I. Lieberman, P. E. Malinowski, D. Cheyns, Z. Hens, *Adv. Sci.* **2022**, *9*, 2200844.

[14] J. Lee, E. Georgitzikis, Y. Li, Z. Lin, J. Park, I. Lieberman, D. Cheyns, M. Jayapala, A. Lambrechts, S. Thijs, R. Stahl, P. E. Malinowski, 2020 IEEE Int. Electron Devices Meeting (IEDM), IEEE, CA, USA **2020**.

[15] G. Konstantatos, E. H. Sargent, *Colloidal Quantum Dot Optoelectronics and Photovoltaics*, Cambridge University Press, Cambridge **2013**.

[16] M. V. Kovalenko, L. Manna, A. Cabot, Z. Hens, D. V. Talapin, C. R. Kagan, V. I. Klimov, A. L. Rogach, P. Reiss, D. J. Milliron, P. Guyot-Sionnnest, G. Konstantatos, W. J. Parak, T. Hyeon, B. A. Korgel, C. B. Murray, W. Heiss, *ACS Nano* **2015**, *9*, 1012.

[17] C. R. Kagan, E. Lifshitz, E. H. Sargent, D. V. Talapin, *Science* **2016**, *353*, aac5523.

[18] M. K. Choi, J. Yang, T. Hyeon, D.-H. Kim, *npj Flexible Electron.* **2018**, *2*, 10.

[19] I. Moreels, Y. Justo, B. De Geyter, K. Haustraete, J. C. Martins, Z. Hens, *ACS Nano* **2011**, *5*, 2004.

[20] R. Sliz, M. Lejay, J. Z. Fan, M.-J. Choi, S. Kinge, S. Hoogland, T. Fabritius, F. P. García de Arquer, E. H. Sargent, *ACS Nano* **2019**, *13*, 11988.

[21] J. P. Clifford, G. Konstantatos, K. W. Johnston, S. Hoogland, L. Levina, E. H. Sargent, *Nat. Nanotechnol.* **2009**, *4*, 40.

[22] M. Vafaie, J. Z. Fan, A. M. Najarian, O. Ouellette, L. K. Sagar, K. Bertens, B. Sun, F. P. García de Arquer, E. H. Sargent, *Matter* **2021**, *4*, 1042.

[23] M. Vafaie, A. Morteza Najarian, J. Xu, L. J. Richter, R. Li, Y. Zhang, M. Imran, P. Xia, H. W. Ban, L. Levina, A. Singh, J. Meitzner, A. G. Pattantyus-Abraham, F. P. García de Arquer, E. H. Sargent, *Proc. Natl. Acad. Sci. USA* **2023**, *120*, e2305327120.

[24] Muhammad, D. Choi, D. H. Parmar, B. Rehl, Y. Zhang, O. Atan, G. Kim, P. Xia, J. M. Pina, M. Li, Y. Liu, O. Voznyy, S. Hoogland, E. H. Sargent, *Adv. Mater.* **2023**, *35*, 2306147.

[25] S. Chatterjee, K. Nemoto, B. Ghosh, H.-T. Sun, N. Shirahata, *ACS Appl. Nano Mater.* **2023**, *6*, 15540.

[26] Y. Wang, L. Peng, J. Schreier, Y. Bi, A. Black, A. Malla, S. Goossens, G. Konstantatos, *Nat. Photonics* **2024**, *18*, 236.

[27] R. Wang, Y. Shang, P. Kanjanaboos, W. Zhou, Z. Ning, E. H., *Energy Environ. Sci.* **2016**, *9*, 1130.

[28] B. K. Jung, H. K. Woo, C. Shin, T. Park, N. Li, K. J. Lee, W. Kim, J. H. Bae, J. P. Ahn, T. N. Ng, S. J. Oh, *Adv. Opt. Mater.* **2022**, *10*, 2101611.

[29] D. Bederak, D. M. Balazs, N. V. Sukharevska, A. G. Shulga, M. Abdu-Aguye, D. N. Dirin, M. V. Kovalenko, M. A. Loi, *ACS Appl. Nano Mater.* **2018**, *1*, 6882.

[30] A. O. Goushcha, B. Tabbert, *Opt. Eng.* **2017**, *56*, 097101.

[31] M. P. Hendricks, M. P. Campos, G. T. Cleveland, I. Jen-La Plante, J. S. Owen, *Science* **2015**, *348*, 1226.

[32] M. Biondi, M. J. Choi, O. Ouellette, S. W. Baek, P. Todorović, B. Sun, S. Lee, M. Wei, P. Li, A. R. Kirmani, *Adv. Mater.* **2020**, *32*, 1906199.

[33] O. Ouellette, N. Hossain, B. R. Sutherland, A. Kiani, F. P. García de Arquer, H. Tan, M. Chaker, S. Hoogland, E. H. Sargent, *ACS Energy Lett.* **2016**, *1*, 852.

[34] C. Giansante, I. Infante, E. Fabiano, R. Grisorio, G. P. Suranna, G. Gigli, *J. Am. Chem. Soc.* **2015**, *137*, 1875.

[35] W. J. Beek, M. M. Wienk, M. Kemerink, X. Yang, R. A. J. Janssen, *J. Phys. Chem. B* **2005**, *109*, 9505.